2024 IEEE/RSJ International Conference on Intelligent Robots and Systems (IROS)
October 14-18, 2024. Abu Dhabi, UAE

A High-Performance Anthropomorphic Robotic Arm for Household Applications

Tianliang Liu, Sicheng Yang, Jingchen Li, Xiangchi Chen, Shuai Wang, Xiao Teng, Wangwei Lee, Xiong Li†, and Yu Zheng, *Senior Member, IEEE*

***Abstract*— Anthropomorphic robotic arms, mimicking the structure and function of human arms, show great potential for helping people in various tedious and repetitive household tasks. However, such arms mostly consist of multiple serial links controlled independently by actuators at joints with high reduction ratios, posing challenges in household services in terms of load capacity, responsiveness, and safety. In this paper, we propose a high-performance anthropomorphic arm called TRX-Arm based on differential cable transmission, characterized by features of high dynamics, high load capacity, and inherent compliance. TRX-Arm is composed of three deferential cable-driven coupling joints and one independent roll joint. Thanks to the cable differential transmission, the joints are capable of achieving doubled torque and stiffness without replacing motors. To enhance safety in human-robot interaction, the actuators including motors, reducer, belt, and pulley are mounted at the shoulder near the base and drive the joints remotely using cables, thereby minimizing the inertia of the whole arm. The workspace of TRX-Arm has a volume of 1.56 m^3, much larger than that of the human arm. Real experiments show its capabilities including high repeatability and load capacity as well as high dynamic behavior of a dual-arm robot platform built with TRX-Arms.**

I. Introduction

Anthropomorphic robotic arms are designed to mimic the structure and function of the human arm [1]–[5], possessing desirable features such as multiple degrees of freedom (DoFs), high dexterity, and human-like movement, with which such arms are promising in various fields, such as manufacturing [3], healthcare [4], space exploration [5], and household service [1]. Generally, anthropomorphic robotic arms consist of multiple serial links for the human-like configuration. Their joints are often controlled independently by actuators, which are composed of motors and reducers and mounted at the joint's centers for the structural compactness [1], [2]. Consequently, this design results in a relatively high inertia for the robotic arm. To reduce the potential risk to humans, such heavyweight robotic arms can only move slowly by utilizing reducers with high ratios, thereby sacrificing high dynamic performance. Additionally, the performance of these independently-driven joints ultimately depends on their motor's performance. Therefore, under the condition of existing serial structure with the same size, it is almost impossible to further enhance the performance of such arms simply by altering the motor selection, posing a great challenge for these types of arms to meet the requirements for services in household environments, which require high dynamics, safety, high payload but lightweight.

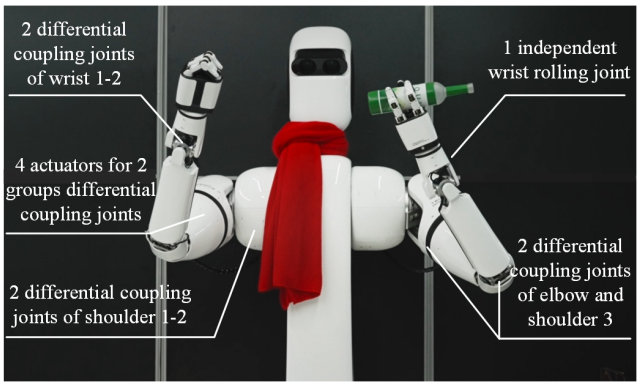

Fig. 1. TRX-Arm: a differential cable-driven arm by Tencent Robotics X. More demonstrations of this robot are shown in the accompanying video.

To improve the performance of anthropomorphic robotic arms without compromising safety, researchers have focused on reducing their inertia by employing remote cable transmission, and then placing the joint actuators near the base to enhance system responsiveness [6]–[12]. Furthermore, to extremely enhance the high dynamic capabilities of the arm, some researchers have proposed lightweight cable reduction mechanisms [13]–[15]. Through cable transmission and reduction, not only can the overall arm's mass be reduced, but the system inertia can also be further reduced, resulting in high dynamic and backdrivability without sacrificing system safety. Nevertheless, the arm's structural stiffness and load capacity are relatively limited and cannot be comparable to that of the human arm.

Another approaches to improve the anthropomorphic robotic arm's performance, including payload and stiffness, is to utilize the differential coupling mechanism. This mechanism enables dynamic combination of the driving torques of actuators, allowing the joint to have n times the torque (n represents the number of differential coupling actuators). Actually, such mechanisms can be categorized into rigid-link mechanisms and flexible transmission mechanisms. The rigid-link mechanisms, which include gear transmission mechanisms and link-based parallel mechanisms [16], exhibit significant advantage of high stiffness and precision. However, they also suffer from many obvious drawbacks, e.g., gear mechanisms are heavy and link-based parallel mechanisms have variable joint-motor ratios and limited joint ranges. On the other hand, the flexible transmission

All the authors are with Tencent Robotics X, Shenzhen, Guangdong 518057, China.
† Corresponding author, E-mails: henricli@tencent.com

mechanism employs flexible materials，such as cables [17]–[20], belts [21], etc., as the transmission medium, enabling it to achieve light weight, and a larger joint ranges with a fixed joint-motor ratio. Specifically, the belt-based differential mechanisms are easy to deploy and maintain without requiring fixation and suitable for low torque transmission applications. However, for high torque transmission applications, wider and thicker belts would be required, leading to a less compact overall structure. In comparison with belt-based mechanisms, the cable-driven differential mechanisms offer much more benefits, such as the flexible arrangement of joint actuators near the base and the capability of high torque transmission.

Inspired by the two approaches mentioned above, we combine the design of remote cable transmission, lightweight cable reduction, and differential mechanism, and propose a high-performance anthropomorphic robotic arm, named TRX-Arm, comparable to a human arm without compromising system safety and dexterity, as shown in Fig. 1. The robotic arm consists of a single independent wrist rolling joint and 3 differential coupling joints. The driving torques of two actuators of each coupling joints can be dynamically combined, allowing the joint to obtain doubled torque and stiffness without replacing motors and further enhancing the arm's load capacity and high dynamic capabilities. Considering the safety interaction between humans and the TRX-Arm, its mass and inertia are carefully designed. Through kinematics analysis, it shows that TRX-Arm has a much larger workspace than a human arm. Furthermore, several typical performance experiments have been conducted to validate the high repeatability and payload, high dynamics capabilities of the robotic arm.

The main contributions of this paper include:

- Present a general conceptual cable differential transmission structure design with detailed modeling;
- Propose a novel differential cable-driven structure for high-performance anthropomorphic arm, TRX-Arm;
- Detail the 3-D model design, prototype the whole arm, and validate its performance.

The rest of this paper is organized as follows. Section II presents the conceptual design of the differential cable-driven structure after the design requirements analysis. Section III details the mechanism design of TRX-Arm with cable differential transmission, including the shoulders, elbow, and wrist. In Section IV, the kinematics model are established for the workspace analysis. Section V reports the performance experiments to verify the repeatability, payload, and dynamic capabilities of TRX-Arm. Section VI concludes this paper.

II. Conceptual Structure Design

A. Design Requirement

Our anthropomorphic robotic arm TRX-Arm is aimed for household environments to conduct various tedious and repetitive household tasks. Given that kitchenware, furniture, electrical appliances, and other items are all tailored for human convenience, it is crucial for TRX-Arm to possess the structure and functionality that mimic the human arm, including load capacity and dynamic response capabilities. In addition, for the safe human-robot interaction, it also needs to be designed with careful considerations of safety. To do so, the following design requirements are deemed essential:

1) *Mimic the configuration of the human arm*: This can help the arm have a workspace comparable to that of the human arm for household services without collision;
2) *Extremely low effective mass and inertia*: It is one of the prerequisites for high dynamics and also ensures safety in human-robot interaction;
3) *High stiffness comparable to the industry robot*: This is benefit for robots to have high precision and be less susceptible to vibration;
4) *High payload comparable to the human arm*: It helps robots have a certain carrying capacity during operations, such as moving and rearranging furniture;
5) *High dynamic capability comparable to the human arm*: It helps robots make quick reactions, such as catching falling objects, and perform high dynamic tasks, such as cooking.

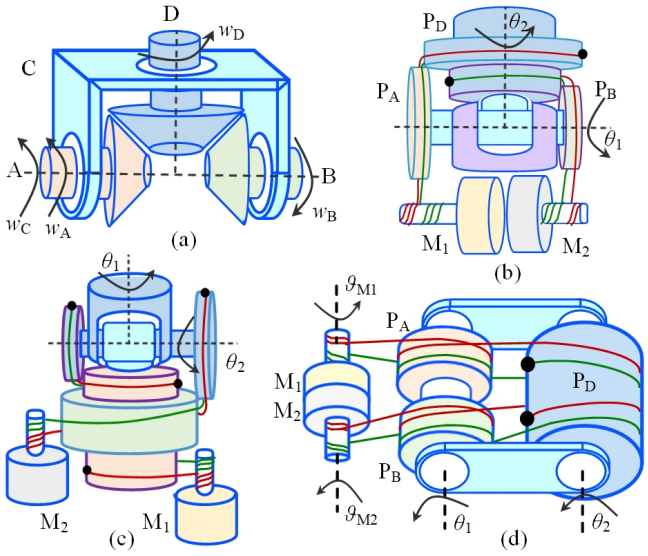

Fig. 2. Different kind of conceptual differential structures. (a) Traditional gear transmission differential structure. (b) Equivalent cable-driven differential structure with crossed axes. (c) Cable-driven differential drive mechanism with another cross axis in the exact reverse order of (b). (d) General cable-driven differential structure with uncrossed axes.

B. Differential Structure Design

1) Modular Structure Design: The typical gear transmission differential mechanism can be simplified as shown in Fig. 2 (a). The entire mechanism includes two inputs components, A and B, which engage with D respectively through gears, thereby transmitting the motions; Meanwhile, C acts as the fixed bracket for D, serving as another output of the structure. For such differential mechanism, there exits

the following kinematics relationships.

$$\begin{bmatrix} w_{\mathrm{A}} \\ w_{\mathrm{B}} \end{bmatrix} = \begin{bmatrix} 1 & -k_{\mathrm{D1}} \\ -1 & -k_{\mathrm{D2}} \end{bmatrix} \begin{bmatrix} w_{\mathrm{C}} \\ w_{\mathrm{D}} \end{bmatrix} \tag{1}$$

where $w_i (i \in \{\mathrm{A}, \mathrm{B}, \mathrm{C}, \mathrm{D}\})$ represents the angular velocities of the component i of the structure, k_{D1} and k_{D2} are the gear reduction ratio between components D and A, D and B respectively. Then, by applying the principle of virtual work, we can obtain:

$$\begin{bmatrix} \tau_{\mathrm{C}} \\ \tau_{\mathrm{D}} \end{bmatrix} = \begin{bmatrix} 1 & -1 \\ -k_{\mathrm{D1}} & -k_{\mathrm{D2}} \end{bmatrix} \begin{bmatrix} \tau_{\mathrm{A}} \\ \tau_{\mathrm{B}} \end{bmatrix} \tag{2}$$

Assume that k_{D1} and k_{D2} are both 1 and τ_{A} and τ_{B} have the maximum value τ_m. Then, we have

$$\max(\mathrm{abs}(\tau_{\mathrm{C}})) = \max(\mathrm{abs}(\tau_{\mathrm{D}})) = 2\tau_m. \tag{3}$$

Therefore, the differential transmission in Fig. 2(a) allows for the dynamic combination of input torques within the mechanism, resulting in a maximum output torque at the joints of up to 2 times.

Leveraging this characteristic of the structure, an equivalent cable-driven differential transmission structure was further designed in Fig. 2(b) with detail cable routing. The output of this structure consists of two intersecting joints, i.e. the pitch and roll joints. The cables on motors M1 and M2, passing over the transition pulleys P_{A} and P_{B} of the pitch axis in the same direction, wind around the pulley P_{D} in opposite directions and finally are fixed on it. Hence, it owns the same motion transmission as well as the feature of dynamic combination as the mechanism in Fig. 2(a).

However, as for the cross axis in the exact reverse order of Fig. 2(b), it will be another differential structure for requirements of both cables and motors rearrangements, as shown in Fig. 2(c). Furthermore, when considering the scenario where two coupling axes are parallel or perpendicular to each other without intersecting, a general cable-driven differential structure is then designed with similar cable routing, as shown in Fig. 2(d).

2) Torque and Stiffness Analysis: Based on the relation 1 and 2, the relationships between joints and motors of such general structure in Fig. 2(d) can be similarly derived as:

$$\begin{bmatrix} \boldsymbol{w}_{\mathrm{M1}} \\ \boldsymbol{w}_{\mathrm{M2}} \end{bmatrix} = \begin{bmatrix} -k_{\mathrm{A}} & -k_{\mathrm{D1}} \\ k_{\mathrm{B}} & -k_{\mathrm{D2}} \end{bmatrix} \begin{bmatrix} w_1 \\ w_2 \end{bmatrix} \tag{4}$$

$$\begin{bmatrix} \tau_1 \\ \tau_2 \end{bmatrix} = \begin{bmatrix} -k_{\mathrm{A}} & k_{\mathrm{B}} \\ -k_{\mathrm{D1}} & -k_{\mathrm{D2}} \end{bmatrix} \begin{bmatrix} \tau_{\mathrm{M1}} \\ \tau_{\mathrm{M2}} \end{bmatrix} \tag{5}$$

where k_{A} and k_{B} are radius ratios of transition pulleys P_{A} and P_{B} to motor shafts respectively, and k_{D1} and k_{D2} are the radius ratios of pulley P_{D} to the motor shafts.

On the other hand, each joint of the coupling modular in Fig. 2(d) can be seen as a two-branch parallel mechanism when their motors are fixed. Assuming stiffness of the corresponding joint with a single branch is K, then joint stiffness of such differential coupling modular is

$$K_{\mathrm{coupling}} = 2K. \tag{6}$$

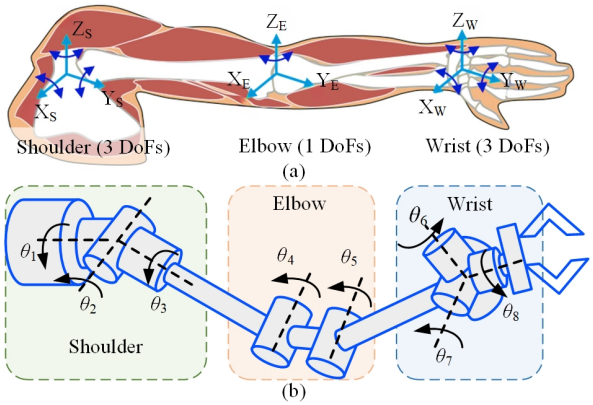

Fig. 3. Configuration design of TRX-Arm. (a) Human arm configuration. (b) The 8-joint 7-DoF human-like configuration of TRX-Arm.

Therefore, with the relationships above, such kind of cable-driven differential transmission coupling modular are capable of similarly achieving a maximum joint torque of up to 2 times. Moreover, the stiffness of such joints can also be double compared to that of independent actuator driving.

III. Mechanical Design

A. Configuration Design

To facilitate cable differential transmission and routing, and maximize the whole arm performance, the configuration of TRX-Arm consists of three differential modules and a separate end roll joint, as illustrated in Fig. 3. Firstly, for the module of shoulder 1-2, the configuration of roll-pitch is much more appropriate for achieving a large joint range rather than pitch-yaw. Then, for the last two differential modules, their actuators are considered to be mounted at shoulder 3 to minimize the inertia of TRX-Arm. Their motions can be transmitted to the controlled joints remotely through cables. For system control simplicity, the cable decoupling design is needed at the elbow. Such 1-DoF decoupling mechanism with cable transmission is a typical rolling joint consisting of two interlinked joints with equal angles [15], [22].

Therefore, featuring an anthropomorphic configuration with a 3-DoF shoulder, a 1-DoF elbow, and a 3-DoF wrist, TRX-Arm has totally 8 joints with 7 active DoFs. Specifically, its elbow consists of two interlinked joints with equal angles and contributes only 1 DoF.

B. Differential Coupling Joints Design

According to the previous differential transmission structure and configuration design, the overall TRX-Arm can be divided into three differential modules: shoulder 1-2, shoulder 3 and elbow, and wrist 1-2, along with a separate end roll joint, which facilitates the differential cable routing of each module. The detailed mechanism designs are presented as follows.

1) Shoulder 1-2: With the roll-pitch configuration, shoulder 1-2 adopts the conceptual differential structure depicted in Fig. 2(c). To improve the driving torque without sacrificing the lightweight, a high power-to-weight ratio motor, i.e.

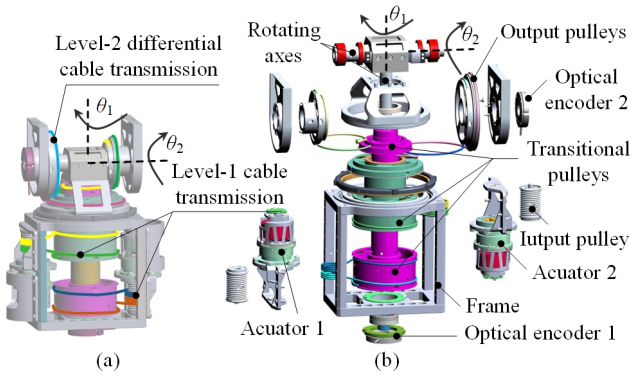

Fig. 4. Differential mechanism design of Shoulder 1-2. (a) Two level cable transmission design. (b) Exploded view of whole shoulder 1-2.

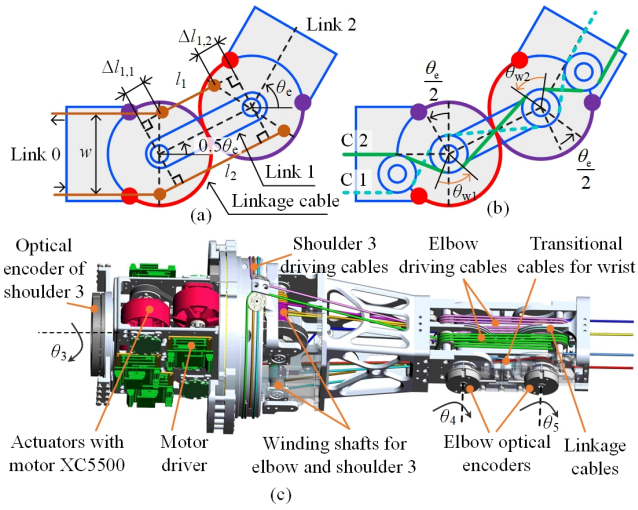

Fig. 5. Design of shoulder 3 and elbow with differential cable mechanism. (a) The principle of elbow cable driving. (b) The decoupling principle of transitional cables at elbow. (c) Detail design of differential cable-driven elbow and shoulder 3.

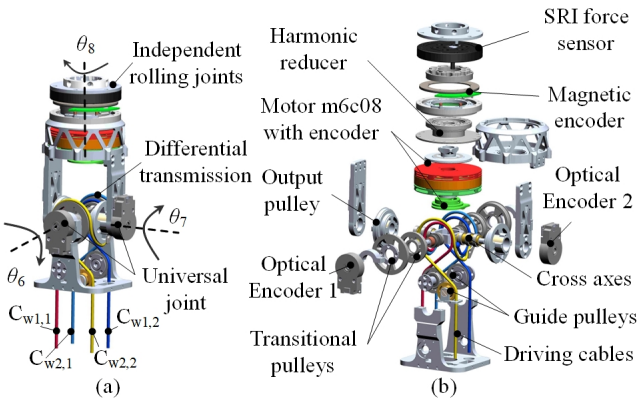

Fig. 6. Wrist design. (a) Overall view of wrist design. (b) Exploded view of the whole wrist.

the outer rotor motor MAD XC5500, is chosen as the actuating motor, equipped with a harmonic reducer of 50:1 reduction ratio and a magnetic encoder. Moreover, a two-level lightweight cable transmission is also implemented for shoulder 1-2, as shown in Fig. 4(a), where the 1st-level cable transmission has a reduction ratio of 1:3 and the 2nd level has a 1:1 differential transmission. On the other hand, high-precision integral optical encoders are integrated at the joints for the precise position control. Then, the detailed mechanism for shoulder 1-2 is depicted in Fig. 4(b).

2) Shoulder 3 and Elbow: Firstly, for elbow design, its driving principle is illustrated in Fig. 5(a). Its two interlinked joints are constrained through linkage cables to ensure consistent angles at any time. At any given joint angle θ_e, the length change of the driving cable l_1 can be calculated as

$$\Delta l_1 = -(\Delta l_{1,1} + \Delta l_{1,2}) = -w \sin(\frac{\theta_e}{2}). \tag{7}$$

Similarly, the length change of another driving cable l_2 can be determined as

$$\Delta l_2 = -\Delta l_1 = w \sin(\frac{\theta_e}{2}). \tag{8}$$

From (7) and (8), the changes of cable lengths, i.e., l_1 and l_2, one-to-one correspond to the joint angle θ_e. Nonetheless, their total lengths remain constant during the movement of rolling joints. Hence, the elbow can be driven by the length control with the cable routing in Fig. 5(a).

Furthermore, to lower the inertia of the arm, wrist actuators are also mounted at shoulder 3. This necessitates the decoupling routing of driving cables passing through the elbow, allowing the transmission of motion to the wrist without affecting the elbow's movement. The decoupling principle is shown in Fig. 5(b). Taking the transitional cable C_1 as an example, it passes through the first joint with a wrap angle of θ_{w1} and then further wraps around the pulley at the second joint with a wrap angle of θ_{w2}. When elbow moves by an angle of θ_e, θ_{w1} decreases by $\theta_e/2$ and θ_{w2} increases by $\theta_e/2$. Hence, their total wrap angles can still remain constant, which further illustrates the decoupling between the movement of elbow and wrist driving cables(i.e. the movement of the wrist 1-2).

Then, based on the configuration design in Fig. 3, the differential structure of two separate joints of shoulder 3 and elbow can then be determined as in Fig. 2(d). Two sets of driving cables are led out from the interior of shoulder 3, pass through the rolling joints at the elbow, and then wind around the cable drums of shoulder 3 in opposite directions. To minimize the overall weight of the arm, two-stage belt and cable reductions are employed in the design of shoulder 3 and the elbow. Specifically, a 3-set movable pulley reduction mechanism with a 6:1 reduction ratio is implemented at the elbow to further enhance joint stiffness and torque. With the integration of high precision optical encoders at each joint, the elbow-shoulder-3 mechanism is shown in Fig. 5(c).

3) Whole Wrist Design: From Fig. 3, the configuration of wrist 1-2 is defined as yaw-pitch, which differs from the configuration depicted in Fig. 2(b). Nevertheless, its differential structure design can still be referenced from Fig. 2(b) due to the actual 90-degree difference in their second joints' initial angles. The pulley D in Fig. 2(b) is designed as two identical output pulleys for convenient cable fixation in the

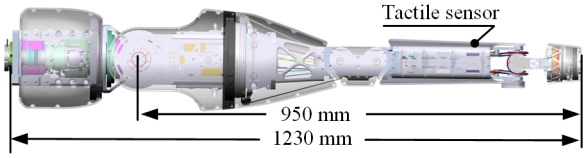

Fig. 7. Overall TRX-Arm with a tactile sensor array on the forearm.

confined space of wrist. To ensure high joint stiffness, two sets of 3 mm diameter steel cables (7 × 19 construction, breaking strength of 5900 N, Dongguan Shuanghe Control Cable Co.) are used for differential transmission, ultimately wrapping around the output pulleys on both sides, as shown in Fig. 6(a). Then, through motion remote transmission and the aforementioned differential transmission, control of wrist 1-2 can be achieved. Specifically, belt and remote cable transmissions are employed in the wrist to achieve a compact actuator layout structure. Moreover, the power-transmission cables of wrist 1-2, passing through the rolling joints at the elbow, are further reduced using movable pulleys in the forearm for improving joint stiffness and torque.

For the separate joint of wrist 3, i.e. the end roll joint, a high power-to-weight ratio outer-rotor motor MAD M6c08 is chosen, equipped with a 50:1 reduction ratio harmonic reducer. Dual magnetic encoders with large hollow are adopted for the convenience of electrical cable routing. Moreover, to ensure safe human-robot interaction, an SRI 6-D F/T sensor is integrated at the end of wrist, which not only enables accurate force sensing but helps prevent high impact between the robotic arm and the environment. The entire wrist with its detailed structure is shown in Fig. 6(b).

C. Whole Arm and Specification

Based on the above design, the shoulder, elbow, and wrist sections of TRX-Arm have been determined. Furthermore, to integrate more diverse sensory information, the forearm is covered with a custom tactile sensor array, which has 768 taxels and a refresh rate of up to 1 kHz. Fig. 7 shows the complete TRX-Arm and Table I lists its specifications.

IV. Kinematics and Workspace Analysis

A. Kinematics Modeling

1) Forward Kinematics: The DH coordinate system of TRX-Arm is established according to the standard DH method, as shown in Fig. 8. The corresponding DH parameters are given in Table. II, by which the local homogeneous transformation matrices ${}^{i}\boldsymbol{T}_{i+1}$ between adjacent coordinate systems can be derived as

$$ {}^{i}\boldsymbol{T}_{i+1} = \begin{bmatrix} {}^{i}\boldsymbol{R}_{i+1} & {}^{i}\boldsymbol{p}_{i+1} \\ \boldsymbol{0} & 1 \end{bmatrix} \tag{9} $$

where ${}^{i}\boldsymbol{R}_{i+1}$ and ${}^{i}\boldsymbol{p}_{i+1}$ are the local transformation and the position between adjacent coordinate systems, respectively.

Based on the mechanical design in Section III, the joints at the elbow are coupled to have equal angles, which yields

$$ \theta_4 = \theta_5 = \frac{\theta_e}{2}. \tag{10} $$

TABLE I. Specifications of TRX-Arm

Items	Specifications	
Dimension (mm)	ϕ 180×950	
Weight (kg)	Overall arm	17.6
	Moving part	8.6
DoFs	Total	7
	Should/Elbow/Wrist	3/1/3
Payload (kg)	6.5 (0.8 arm length, with hand)	
Equivalent Reduction Ratio	Shoulder	150, 150, 92
	Elbow	92–130
	Wrist	50, 50, 50
Max Torque (N·m)	Shoulder	153, 153, 94
	Elbow	96–134
	Wrist	51
Max Speed (rpm)	Shoulder	65, 65, 108
	Elbow	108–77
	Wrist	200
Actuators	MAD XC5500 (Shoulder, Elbow and Wrist 1-2)	
	MAD M6c08 (Wrist 3)	
Sensors	Tactile sensor array with 768 taxels (Forearm)	
	SRI 6-D F/T sensor (Wrist)	

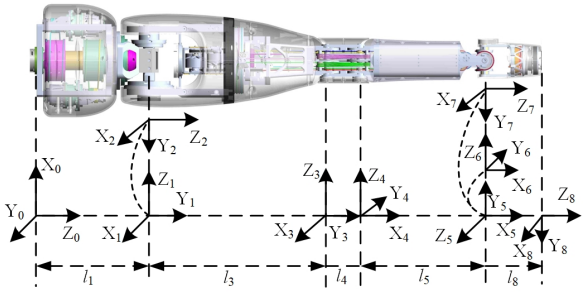

Fig. 8. DH coordinate system of TRX-Arm.

Then, the forward kinematics of the 7-DoF TRX-Arm can be described as

$$ \begin{aligned} \boldsymbol{f}(\tilde{\boldsymbol{\Theta}}) &= {}^{1}\boldsymbol{T}_{2}^{2}\boldsymbol{T}_{3}\left({}^{3}\boldsymbol{T}_{4}^{4}\boldsymbol{T}_{5}\right)^{5}\boldsymbol{T}_{6}^{6}\boldsymbol{T}_{7}^{7}\boldsymbol{T}_{8} \\ &= \boldsymbol{f}(\tilde{\theta}_1, \tilde{\theta}_2, \tilde{\theta}_3, \ldots, \tilde{\theta}_7) \end{aligned} \tag{11} $$

$$ \tilde{\theta}_i = \begin{cases} \theta_i & i < 4 \\ 2\theta_i & i = 4 \\ \theta_{i+1} & 4 < i \leq 7 \end{cases} \tag{12} $$

where $\tilde{\theta}_i$ is the equivalent angle of joint i corresponding to the i-th DoF of TRX-Arm.

2) Inverse Kinematics: Having 8 joints and 7 independent DoFs, TRX-Arm is a redundant manipulator, for which the least squares method based on the pseudo-inverse of the Jacobian matrix is one of the most common methods for solving inverse kinematics. Based on (11), the Jacobian matrix of TRX-Arm can be derived and written as

$$ \boldsymbol{J} = \begin{bmatrix} \tilde{v}_1 & \tilde{v}_2 & \cdots & \tilde{v}_7 \\ \tilde{w}_1 & \tilde{w}_2 & \cdots & \tilde{w}_7 \end{bmatrix} \in \boldsymbol{R}^{6\times 7} \tag{13} $$

where $\tilde{v}_i$ and $\tilde{w}_i$ represent the impacts of unit angular velocities of 7 independent DoFs $\tilde{\theta}_i$ on the linear and angular velocities of the end-effector, respectively. Based on the relation (10), they can be calculated as

$$ \tilde{v}_i = \begin{cases} v_i & i < 4 \\ \frac{1}{2}(v_i + v_{i+1}) & i = 4 \\ v_{i+1} & 4 < i \leq 7 \end{cases} \tag{14} $$

TABLE II. DH Parameters of TRX-Arm

Link i	a_i(mm)	$\alpha_i(^\circ)$	d_i(mm)	$\theta_i(^\circ)$
1	0	90	l_1	$90+\theta_1$
2	0	-90	0	θ_2
3	0	90	l_3	θ_3
4	l_4	0	0	$90+\theta_4$
...	...	...	...	...
8	0	0	l_8	θ_8

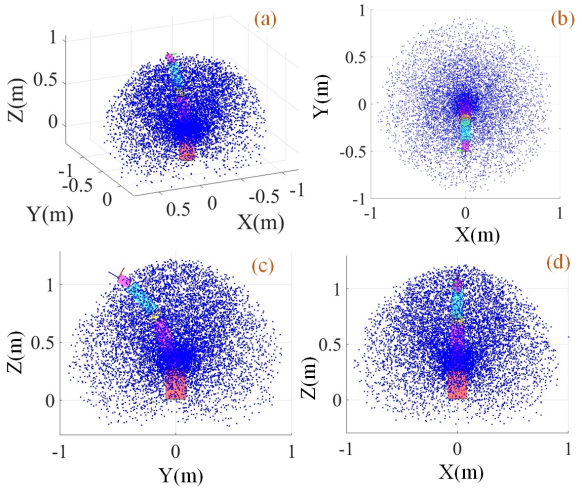

Fig. 9. Workspace of TRX-Arm. (a) Axis side view. (b) XY-plane view. (c) YZ-plane view. (d) XZ-plane view.

$$\tilde{w}_i = \begin{cases} w_i & i < 4 \\ \frac{1}{2}(w_i + w_{i+1}) & i = 4 \\ w_{i+1} & 4 < i \leq 7 \end{cases} \tag{15}$$

where v_i and w_i correspond to the real 8 joints of TRX-Arm.

B. Workspace Analysis

Based on the kinematics model established above, the workspace of TRX-Arm can be calculated based on the Monte-Carlo method as

$$\boldsymbol{W} = \boldsymbol{p}_e(\tilde{\theta}_1, \tilde{\theta}_2, \tilde{\theta}_3, \ldots, \tilde{\theta}_7) \begin{cases} \tilde{\theta}_i^{min} \leq \tilde{\theta}_i \leq \tilde{\theta}_i^{max} \\ i = 1, 2, 3, \ldots, 7 \end{cases} \tag{16}$$

where $\boldsymbol{p}_e$ is the position of the end-effector of TRX-Arm. Fig. 9 shows the workspace of TRX-Arm, which reaches a volume of 1.56 m^3, much larger than that of the human arm (i.e., 0.667 m^3 [23]). This is because the workspace of the human arm behind the body is very small, while TRX-Arm's workspace is symmetric in front and rear [see Fig. 9(c)]. However, the front portion of TRX-Arm's workspace is still larger than that of the human arm's. The comparison of TRX-Arm with other popular commercial robotic arms is shown in Table. III.

V. Performance Experiments

To verify the performance of the proposed TRX-Arm, a prototype was built with Ethercat communication. Experiments with focuses on positioning repeatability, load capacity, and dynamic motion were conducted on the prototype. Demonstrations are also shown in the accompanying video.

TABLE III. Comparison of TRX-Arm and Commercial Arms

	TRX-Arm	ABB 1100	Kinova Gen3	UR5e
Workspace (m^3)	1.565	0.164	0.650	0.888
Dex. WS (m^3)	1.124	0.097	0.432	0.799
GMI*	0.155	0.012	0.041	0.058

GMI*: Global manipulability index.

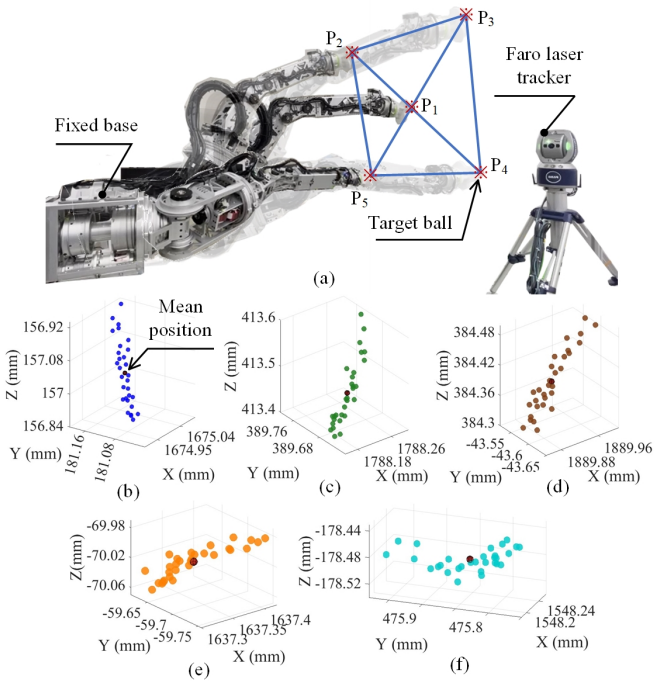

Fig. 10. Repeatability test of TRX-Arm. (a) 5 pre-defined target positions P_1–P_5 for the test. (b)–(f) Point cloud at P_1–P_5.

A. Position Repeatability

The repeatability test of TRX-Arm was conducted with closed-loop position control at every joint, referring to the performance criteria and related test methods of ISO 9283. As shown in Fig. 10(a), the position of TRX-Arm's end-effector in space is measured using a Faro laser tracker, which has an accuracy of 0.01 mm. The measurement results at 5 pre-defined positions for 30 times are shown in Fig. 10(b)-(f). Then, the mean positions for each target position can be obtained and used to calculate the average distance $\bar{l}_i$. The 3-sigma distance between the mean and measured positions, i.e., the position repeatability of TRX-Arm, is computed as

$$S_{li} = \sqrt{\frac{\sum_{j=1}^{n}(l_{i,j} - \bar{l}_i)^2}{n-1}} \tag{17}$$

$$RP_{li} = \bar{l}_i + 3S_{li} \tag{18}$$

$$\boldsymbol{RP}_l = [\ 0.174 \quad 0.157 \quad 0.15 \quad 0.11 \quad 0.14\ ] \tag{19}$$

$$\bar{RP}_l = \frac{\sum_{i=1}^{m} RP_{li}}{m} = 0.148 \tag{20}$$

where $l_{i,j}$ ($i \in [1,5]$, $j \in [1,30]$) is the distance between the recorded position j and the mean position i, S_{li} and RP_{li} are the corresponding standard deviation and position

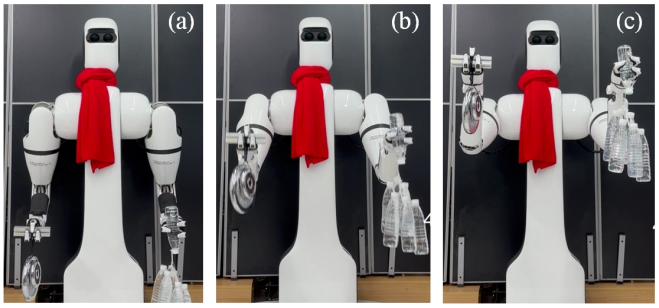

Fig. 11. Load capacity experiment of TRX-Arm.

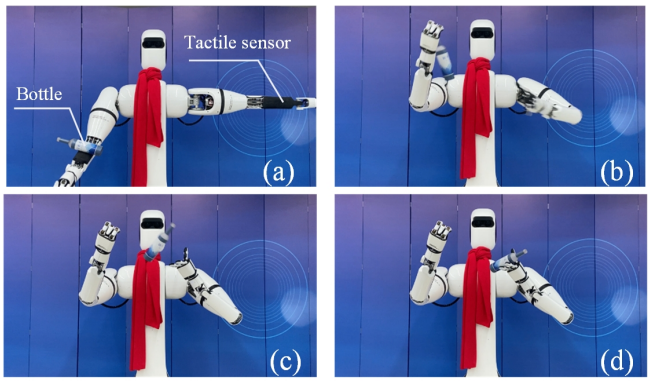

Fig. 12. Bottle throw-catch experiment of TRX-Arm.

repeatability of pre-defined position i, respectively. Finally, the average position repeatability of TRX-Arm is calculated to be 0.148 mm, which is close to the industrial arms (e.g., the positioning repeatability of Kuka's iiwa is 0.1 mm).

B. Load Capacity

Load capacity is one of the important indicators of robotic arms. As shown in Fig. 11, a dual-arm system has been built with two TRX-Arms, each equipped with a three-finger 8-DoF hand called TRX-Hand3, which was also developed by Tencent Robotics X. A standard weight of 6.5 kg and a bundle of bottle water with a similar total weight are held by either hand. Starting with an initial 90° bend at the elbow, TRX-Arm successfully lifted the weight to the highest position. During the while lifting process, the arm extended to approximately 4/5 of its full length, which is consistent with the configuration of the human arm in most tasks in the household environment. Furthermore, with a load capacity of 6.5 kg, TRX-Arm demonstrates the comparable capability to humans in performing the majority of household chores.

C. Dynamic Motion

To verify the dynamic motion capability of TRX-Arm, a bottle throw-catch experiment was designed, as shown in Fig. 12. The bottle is initially placed at a random position on the forearm, which is covered with a tactile sensor array. With the aid of tactile servoing control [24], TRX-Arm tilts back and forth and rolls the bottle on the forearm to a predetermined position for throwing. Once ready, the whole arm starts to swing and accelerates the bottle from a stationary state to approximately 3.5 m/s. After flying out from the forearm, the bottle reaches a maximum height of 0.3 m and is caught by the left hand in about 0.4 s. It is worth mentioning that 3.5 m/s only represents the motion capacity of TRX-Arm's forearm. Its end-effector in the test has a maximum speed of 7.4 m/s and a maximum acceleration of 4.5 m/s^2, comparable to the human arm whose average maximum speed is 7 m/s.

VI. Conclusions

A high-performance anthropomorphic robotic arm is proposed in this paper comparable to the human arm without compromising system safety and dexterity by the combination design of remote cable transmission, lightweight cable reduction, and differential mechanism. The robotic arm consists of three differential coupling modules and a independent wrist roll joint, featuring high load capacity, high dynamics, and inherent compliance. The driving torques of two actuators of each coupling joints can be dynamically combined, allowing the joints to achieve double torque and stiffness without replacing motors and further enhancing the arm's load capacity and high dynamic capabilities. Considering the safety interaction between humans and the arm, its mass and inertia are carefully designed. The capabilities of the robotic arm, including high repeatability, high payload, and high dynamic response have been verified with experiments.

Acknowledgment

The authors would like to thank Kun Xiong, Minhua Sheng, and Zhaohui An for helps with the mechanism design and the system integration.

References

[1] T. Asfour, M. Waechter, L. Kaul, S. Rader, P. Weiner, S. Ottenhaus, R. Grimm, Y. Zhou, M. Grotz, and F. Paus, "Armar-6: A high-performance humanoid for human-robot collaboration in real-world scenarios," *IEEE Robotics & Automation Magazine*, vol. 26, no. 4, pp. 108–121, 2019.

[2] S. Rader, L. Kaul, H. Fischbach, N. Vahrenkamp, and T. Asfour, "Design of a high-performance humanoid dual arm system with inner shoulder joints," in *2016 IEEE-RAS 16th International Conference on Humanoid Robots (Humanoids)*. IEEE, 2016, pp. 523–529.

[3] Wikipedia contributors, "Optimus (robot) — Wikipedia, the free encyclopedia," https://en.wikipedia.org/w/index.php?title=Optimus_(robot)&oldid=1210150836, 2024, [Online; accessed 29-February-2024].

[4] Barrett Technology, Inc., "Wam arm-barrett," https://barrett.com/wam-arm, 2024, [Online; accessed 29-February-2024].

[5] Z. Jiang, S. Liu, H. Li, Q. Dong, X. Chen, and Q. Huang, "Mechanism design and system control for humanoid space robot movement using a simple gravity-compensation system," *International Journal of Advanced Robotic Systems*, vol. 10, no. 11, p. 389, 2013.

[6] S. Mori, K. Tanaka, S. Nishikawa, R. Niiyama, and Y. Kuniyoshi, "High-speed and lightweight humanoid robot arm for a skillful badminton robot," *IEEE Robotics and Automation Letters*, vol. 3, no. 3, pp. 1727–1734, 2018.

[7] Mori, Shotaro and Tanaka, Kazutoshi and Nishikawa, Satoshi and Niiyama, Ryuma and Kuniyoshi, Yasuo, "High-speed humanoid robot arm for badminton using pneumatic-electric hybrid actuators," *IEEE Robotics and Automation Letters*, vol. 4, no. 4, pp. 3601–3608, 2019.

[8] J.-Y. Kuan, K. A. Pasch, and H. M. Herr, "A high-performance cable-drive module for the development of wearable devices," *IEEE/ASME Transactions on mechatronics*, vol. 23, no. 3, pp. 1238–1248, 2018.

[9] T. Liu, W. Xu, T. Yang, and Y. Li, "A hybrid active and passive cable-driven segmented redundant manipulator: Design, kinematics, and planning," *IEEE/ASME Transactions on Mechatronics*, vol. 26, no. 2, pp. 930–942, 2021.

[10] T. Liu, Z. Mu, W. Xu, T. Yang, K. You, H. Fu, and Y. Li, "Improved mechanical design and simplified motion planning of hybrid active and passive cable-driven segmented manipulator with coupled motion," in *2019 IEEE/RSJ International Conference on Intelligent Robots and Systems (IROS)*. IEEE, 2019, pp. 5978–5983.

[11] T. Liu, Z. Mu, H. Wang, W. Xu, and Y. Li, "A cable-driven redundant spatial manipulator with improved stiffness and load capacity," in *2018 IEEE/RSJ International Conference on Intelligent Robots and Systems (IROS)*, 2018, pp. 6628–6633.

[12] Y. Tsumaki, Y. Suzuki, N. Sasaki, E. Obara, and S. Kanazawa, "A 7-dof wire-driven lightweight arm with wide wrist motion range," in *2018 IEEE/RSJ International Conference on Intelligent Robots and Systems (IROS)*. IEEE, 2018, pp. 1–9.

[13] Y.-J. Kim, J.-I. Kim, and W. Jang, "Quaternion joint: Dexterous 3-dof joint representing quaternion motion for high-speed safe interaction," in *2018 IEEE/RSJ International Conference on Intelligent Robots and Systems (IROS)*. IEEE, 2018, pp. 935–942.

[14] H. Song, Y.-S. Kim, J. Yoon, S.-H. Yun, J. Seo, and Y.-J. Kim, "Development of low-inertia high-stiffness manipulator lims2 for high-speed manipulation of foldable objects," in *2018 IEEE/RSJ International Conference on Intelligent Robots and Systems (IROS)*. IEEE, 2018, pp. 4145–4151.

[15] Y.-J. Kim, "Anthropomorphic low-inertia high-stiffness manipulator for high-speed safe interaction," *IEEE Transactions on robotics*, vol. 33, no. 6, pp. 1358–1374, 2017.

[16] Y. Sim and J. Ramos, "Tello leg: The study of design principles and metrics for dynamic humanoid robots," *IEEE Robotics and Automation Letters*, vol. 7, no. 4, pp. 9318–9325, 2022.

[17] J. Heinzmann and A. Zelinsky, "The safe control of human-friendly robots," in *Proceedings 1999 IEEE/RSJ International Conference on Intelligent Robots and Systems. Human and Environment Friendly Robots with High Intelligence and Emotional Quotients (Cat. No. 99CH36289)*, vol. 2. IEEE, 1999, pp. 1020–1025.

[18] W. Li, Y. Wang, S. Togo, H. Yokoi, and Y. Jiang, "Development of a humanoid shoulder based on 3-motor 3 degrees-of-freedom coupled tendon-driven joint module," *IEEE Robotics and Automation Letters*, vol. 6, no. 2, pp. 1105–1111, 2021.

[19] W. Li, P. Chen, D. Bai, X. Zhu, S. Togo, H. Yokoi, and Y. Jiang, "Modularization of 2-and 3-dof coupled tendon-driven joints," *IEEE Transactions on Robotics*, vol. 37, no. 3, pp. 905–917, 2020.

[20] T. Chen, R. Casas, and P. S. Lum, "An elbow exoskeleton for upper limb rehabilitation with series elastic actuator and cable-driven differential," *IEEE Transactions on Robotics*, vol. 35, no. 6, pp. 1464–1474, 2019.

[21] D. V. Gealy, S. McKinley, B. Yi, P. Wu, P. R. Downey, G. Balke, A. Zhao, M. Guo, R. Thomasson, A. Sinclair *et al.*, "Quasi-direct drive for low-cost compliant robotic manipulation," in *2019 International Conference on Robotics and Automation (ICRA)*. IEEE, 2019, pp. 437–443.

[22] Y.-J. Kim, Y. Lee, J. Kim, J.-W. Lee, K.-M. Park, K.-S. Roh, and J.-Y. Choi, "Roboray hand: A highly backdrivable robotic hand with sensorless contact force measurements," in *2014 IEEE International Conference on Robotics and Automation (ICRA)*, 2014, pp. 6712–6718.

[23] N. Klopčar and J. Lenarčič, "Kinematic model for determination of human arm reachable workspace," *Meccanica*, vol. 40, pp. 203–219, 2005.

[24] S. Wang, Y. Huang, W. W. Lee, T. Liu, X. Teng, Y. Zheng, and Q. Li, "A robust model predictive controller for tactile servoing," in *2024 IEEE International Conference on Robotics and Automation (ICRA)*, 2024, accepted.